Sensors and Materials, Vol. 38, No. 11 (2026) 6437–6454
MYU Tokyo

S & M 4689

Water Cut Measurement of Oil–Water Two-phase System Using Helical Uniform Sensing Structure

Haiming Xie,* Rui Wang, and Jianqiang Huang

School of Electronic Engineering, Xi'an Shiyou University, Xi'an China

(Received July 28, 2026; accepted September 24, 2026)

Keywords: helical uniform sensing structure, volumetric homogenization, orthogonal experiment, multiphase flow

Aiming at the limitations of capacitive sensors for water cut measurement in oil–water two-phase systems, including restricted electric field coverage and uneven spatial response, we proposed a helical uniformly distributed sensing structure with a three-dimensional helical configuration in this work. By extending the effective acting path of electrodes, the proposed structure expands the spatial coverage of the sensing zone and homogenizes the electric field distribution within the detection region, which further improves the consistency of capacitive responses induced by variations in oil—water dielectric properties. A three-dimensional finite element model is established using COMSOL Multiphysics software, and an orthogonal experimental design is adopted to optimize the key structural parameters of the helix. Comparative analyses are carried out between the developed structure, an 8-electrode configuration, and a wall-mounted helical structure. Guided by the optimized simulation results, static experimental tests are implemented on oil–water mixtures with varying water cuts to validate the sensing performance of the proposed structure in capturing dielectric variations of oil–water media. The experimental results demonstrate that the three-dimensional helical uniformly distributed sensing structure achieves higher average sensitivity and wider measurement while maintaining favorable linearity and stable output signals. Great consistency between experimental measurements and simulation predictions is observed in terms of variation trends and relative performance. This work provides an effective structural design strategy for water cut detection in oil–water mixtures and multiphase flow parameter measurement.

1. Introduction

Multiphase flow is ubiquitous in petroleum engineering. The accurate measurement of phase content and flow patterns is crucial for optimizing production and ensuring operational safety.(1) However, the strong nonlinearity, transient characteristics, and complex interphase interactions inherent in multiphase flow(2) make it challenging for traditional sensor structures to achieve

*Corresponding author: e-mail: haimingxie@xsyu.edu.cn
https://doi.org/10.18494/SAM6551

ISSN 0914-4935 © MYU K.K.

spatially uniform measurements. This has driven the development of homogenized, high-precision sensing structures. Therefore, this study is focused on the measurement of water cut in oil–water systems by using a capacitive sensing approach.

Existing research primarily relies on traditional coaxial electrode sensor structures[3] with a relatively mature application foundation under relatively stable conditions, such as fully oil- or water-filled media. Capacitive tomography techniques based on circumferential electrode arrays are also widely used for phase distribution reconstruction.[4,5] Although subsequent optimizations improved the radial uniformity of the sensitive field within the detection zone,[6–8] these advancements still rely on the assumption of relatively stable axial distribution within the medium. A typical characteristic is low sensitivity near the pipe center and excessively high sensitivity near the pipe wall. Increasing electrode density can mitigate this issue,[9] but simultaneously leads to a sharp increase in data volume, reduced real-time performance, and intensified coupling interference.

Microwave-based detection technologies have also been applied to water cut measurement using various electrode configurations, including coaxial and multiring structures.[10,11] These methods rely on the propagation characteristics of electromagnetic waves within the medium and demand the high continuity and stability of the medium within the detection zone. To expand the electric field coverage, researchers proposed a planar spiral edge field sensor design.[12] However, its applicability in multiphase flow detection scenarios remains limited. In recent years, arm-spiral structures have been demonstrated to enhance the sensor's resistance to flow pattern interference.[13,14] Nevertheless, the fabrication process for such structures is highly complex and poses significant manufacturing challenges.

In summary, although the aforementioned ring-, array-, and spiral-type sensors employ different electrode layout strategies, their sensing units are all constructed on cylindrical pipe structures. Essentially, they remain optimizations and variations of electrode configurations on cylindrical substrates.

In this paper, we propose a uniformly distributed sensing structure. Through orthogonal parameter simulation experiments, the key parameters of this structure were optimized and screened. Simulation performance comparisons with existing sensor structures were conducted and ultimately validated through practical testing. This uniformly distributed helical sensing structure demonstrates favorable feasibility and outstanding performance, providing a novel solution for multiphase flow parameter detection.

2. Helical Uniformly Distributed Sensing Structure (HUS) and Design

2.1 HUS and design approach

To address the issues of fluid uneven distribution and measurement imbalance in traditional cylindrical capacitive sensors for multiphase flow detection, we propose a helical uniform sensing structure. This structure employs a three-dimensional helical electrode configuration, expanding the effective interaction area between the electrode and the fluid within a finite axial length to achieve a more uniform electric field distribution within the detection zone. By

forming a helical detection cavity between the insulating layer and the return electrode, it enables the sensing of the volumetric distribution of multiphase fluids, structurally mitigating the impact of flow pattern fluctuations on measurement results.

The overall geometry and radial cross-sectional dimensional annotations of the sensor are illustrated in Fig. 1, in which H represents the total axial height of the helical electrodes and p denotes the axial pitch of the helix. Detail a shows a magnified local view of the helical cross section, where R1, R2, and R3 correspond to the radial radii of the helical fluid chamber, shielding layer, and helical electrode, respectively.

Key parameters of the helical uniform sensing structure are summarized in Table 1. The proportionality coefficient denotes the ratio between the spiral electrode radius and the spiral fluid reservoir cross-sectional radius. The overall sensor radius is set to 50 mm.[15] The total radius of this uniform sensing structure satisfies the following equation:

$$r_1 + R_1 = 50 \text{ mm}. \tag{1}$$

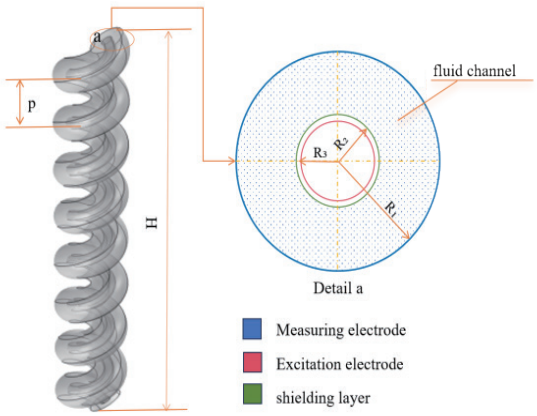


Fig. 1. (Color online) Overall geometry and radial cross-sectional dimensional annotations of the sensor.

Table 1
Main parameters of HUS.

Parameter	Explanation
p_1	Proportional coefficient
R_2	Shield radius
N	Number of turns
r_1	Helical major radius
H	Helical appearance height
R_1	Helical reservoir cavity cross-sectional radius
R_3	Spiral electrode cross-sectional radius
p	Axial pitch of spiral body

2.2 Theory and governing equations of HUS

2.2.1 Governing equations for numerical simulation

To verify the aforementioned theoretical model, a three-dimensional finite element model was established using COMSOL Multiphysics. The electric currents interface in the frequency domain was employed to calculate the electric potential and electric field distributions under low-frequency AC excitation. Under the quasi-static approximation, electromagnetic wave propagation effects can be neglected, and the electric field distribution in the sensing region can be determined from the corresponding frequency-domain governing equations. The capacitance was then obtained from the electrical response of the sensing electrodes.

The steady-state current continuity governing equation in the frequency domain is derived as

$$\nabla\left[\left(\sigma + jw\varepsilon\right)\nabla V\right] = 0\,, \tag{2}$$

where σ denotes the medium conductivity (S/m); $\omega = 2\pi f$ represents the excitation angular frequency (rad/s); $\varepsilon = \varepsilon_0\varepsilon_r$ is the absolute permittivity of the medium (F/m); and j stands for the imaginary unit.

After solving the electric field to obtain the spatial potential distribution, the sensor equivalent capacitance is extracted from the admittance of the excitation electrode, with the calculation formula given below.

$$C = \frac{imag(Y)}{\omega} \tag{3}$$

Here, C is the sensor capacitance, Y is the electrode admittance, and ω is the excitation angular frequency in rad/s. This formula enables the accurate extraction of the sensor capacitance response under various oil–water volume fractions for the calculation of simulation results.

2.2.2 Theoretical model of HUS

On the basis of the conventional capacitance relationship and the geometric configuration of the proposed helical sensing structure, the total capacitance expression was derived in this study as

$$C = \frac{2\pi\varepsilon_0\varepsilon_1\varepsilon_2 P}{A\varepsilon_2 + B\varepsilon_1}, \tag{4}$$

where P denotes the unfolded length of the helical electrode; A and B represent the radial logarithmic geometric coefficients of the sensor structure, respectively; ε_0 is the permittivity of

free space; ε_1 and ε_2 are the relative permittivities of the liquid and shielding layer media, correspondingly.

$$\begin{cases} P = N * \sqrt{(2\pi r_1)^2 + (p)^2} \\ A = \ln(R_1 / R_2) \\ B = \ln(R_2 / R_3) \end{cases} \tag{5}$$

In Eq. (5), N is the number of helical turns, r_1 is the mean radius of a single helical turn, and p is the axial pitch.

2.2.3 Oil–water two-phase mixed dielectric model

The oil–water two-phase fluid inside the pipeline is regarded as a homogeneously mixed medium, and the volume-weighted equivalent permittivity model is expressed as

$$\varepsilon_{1=}\varepsilon_o * (1 - \alpha) + \varepsilon_w * \alpha, \tag{6}$$

where ε_1 is the equivalent permittivity of the oil–water mixture, ε_o is the relative permittivity of the oil phase (soybean oil), ε_w denotes the relative permittivity of the water phase, and α represents the volumetric water cut with a range of $0 \leq \alpha \leq 1$. Variations in water cut alter the component ratio of the oil–water two-phase mixture, which indirectly changes the equivalent permittivity of the mixed medium and eventually leads to a shift in output capacitance. This constitutes the core working mechanism of the proposed sensor for water cut measurement.

In practical oil–water two-phase systems, the effective permittivity depends not only on the phase volume fractions but also on the spatial topology of the dispersed and continuous phases, droplet size, and the characteristic dimensions of the sensing region. Different effective-medium models, including linear and inverse mixture rules, may therefore yield different equivalent permittivities under different phase distributions. In the present study, the oil–water mixture is approximated as a homogeneous effective medium, and the volume-weighted linear mixing model is adopted to establish a controlled relationship between water cut and dielectric permittivity. This assumption is appropriate for the present simulation objective, which focuses on evaluating the structural response and spatial sensitivity of the sensor rather than resolving individual droplets or flow patterns. The effect of actual phase distribution is further considered as a potential source of discrepancy between the idealized simulation and static experimental results.

2.3 Orthogonal experimental design method for optimizing parameters

To determine the optimal structural parameters for uniform distribution sensors, a parametric orthogonal experimental design[15,16] was employed. A three-level orthogonal parameter simulation was conducted, yielding the orthogonal table $L_9(3^4)$, as detailed in Table 2.

Table 2
Three-dimensional simulation test plan.

Experiment ID	Factor		
	Proportionality coefficient p_1	Major radius r_1 of spiral structure (mm)	Number of turns N
1	1.5	40	3
2	1.5	25	6
3	1.5	10	8
4	3	40	6
5	3	25	8
6	3	10	3
7	5	40	8
8	5	25	3
9	5	10	6

2.4 Simulation model and boundary condition setup

All simulations in this work are performed using COMSOL Multiphysics 6.2 with the frequency-domain electric currents module. The excitation voltage is set to 3.3 V and the operating frequency is 1 MHz. The multifrontal massively parallel sparse direct solver (MUMPS) is adopted, and the convergence tolerance is specified as 10^{-6}.

A three-dimensional model was constructed in COMSOL simulation software.[16,17] Free tetrahedral meshes are applied to the model, with local mesh refinement implemented for the helical electrodes and shielding layers. The total number of mesh elements is approximately 210000. The mesh distribution is presented in Fig. 2.

Geometric dimensions are assigned in accordance with the orthogonal parameters listed in Table 2. Uniform boundary conditions are configured for all simulation cases: an alternating voltage is applied to the excitation electrodes, while the outer electrodes are grounded.

Two groups of parametric sweep simulations are carried out: first, orthogonal experimental simulations of structural parameters are conducted following the parameters in Table 2; second, the water cut ranging from 0 to 1 is swept at increment steps of 0.1.

Uniform electrical parameters of media in each region are adopted from the material properties in Table 3. The parameters of the oil–water two-phase medium are updated in real time via the volume-weighted dielectric model.

3. Simulation Results and Performance Analysis

3.1 Evaluation metrics for sensor structure optimization

To quantitatively evaluate structural-parameter effects on sensor performance and set unified optimization criteria, four metrics (sensitivity, sensitivity dispersion, relative sensitivity deviation, and capacitance variation range) are used for structure comparison. They describe sensor response to water-cut variation, spatial-position response consistency, and effective capacitance response range.

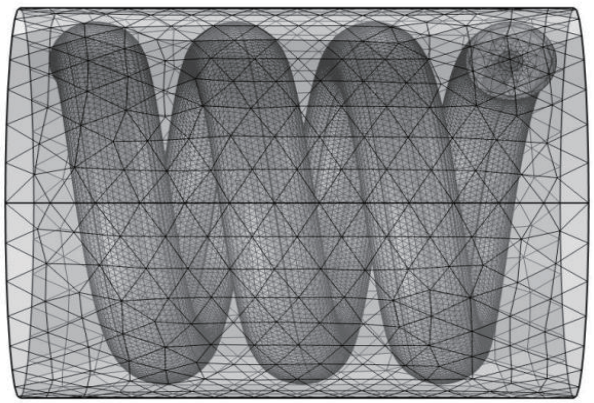


Fig. 2. Mesh diagram of the uniform sensor structure simulation model.

Table 3
Properties of materials.

Material	Application position	Actual relative permittivity	Permittivity assigned in simulation
Soybean oil	Oil-phase fluid medium	2.8–3.0	3
Tap water	Water-phase fluid medium	75–80	80
Aluminum foil	Helical electrode	—	—
PTFE heat-shrink tube	Shielding layer	2.0–2.1	2
UV-curable resin	Pipe outer casing	3.3–4.0	3.5

Let C_i denote the capacitance at water cut α_i for a spatial sampling position and C_0 the reference capacitance at reference water cut α_0. For adjacent water-cut intervals, the local sensitivity for the i-th sampling state is defined as

$$S_i = \frac{c_i - c_0}{a_i - a_0}, \tag{7}$$

where S_i is the capacitance change per unit water-cut variation, representing the sensor response under this condition. The average sensitivity across all sampling positions is adopted to evaluate global response.

$$S_{avg} = \frac{1}{n}\sum_{i=1}^{n} S_i \tag{8}$$

Here, n is the number of spatial sampling points. To evaluate the spatial consistency of the sensing response, the standard deviation of local sensitivity is defined as

$$S_{dvp} = \sqrt{\frac{1}{n-1}\sum_{i=1}^{n}(S_i - S_{avg})^2}\ , \tag{9}$$

where S_{dvp} quantifies the spatial dispersion of local sensitivity relative to S_{avg}. Note that S_{dvp} is not the standard deviation from repeated simulations or experiments; it reflects the spatial uniformity of sensor sensitivity. Smaller S_{dvp} corresponds to more consistent responses across positions.

Since S_{dvp} is affected by the magnitude of S_{avg}, relative sensitivity deviation is introduced for normalized uniformity evaluation.

$$S_{vp} = \frac{S_{dvp}}{\left|S_{avg}\right|} \times 100\% \tag{10}$$

Here, S_{vp} is dimensionless and gives the ratio of sensitivity dispersion to average sensitivity. Lower S_{vp} implies smaller spatial relative-sensitivity differences and higher spatial-response consistency.

Furthermore, the capacitance variation range defines the effective capacitance output over the full water-cut range.

$$\Delta C = C_{max} - C_{min} \tag{11}$$

Here, C_{max} and C_{min} are the maximum and minimum capacitances within the studied water-cut interval, and ΔC is in pF.

Because the three structures employ different electrode topologies, their capacitance depends differently on electrode clearance, electrode geometry, and effective electrode area. Therefore, a single analytical normalization simultaneously incorporating these parameters cannot be defined consistently for all three structures. In contrast, the effective sensing length provides a common and directly measurable geometric parameter for the three configurations. Accordingly, the normalized capacitance is defined as

$$C_L = \frac{C}{L_{eff}}, \tag{12}$$

where C_L is the capacitance per unit effective sensing length and L_{eff} is the effective sensing length. To reduce the effect of sensor scale on the comparison, the capacitance variation was therefore normalized by the effective sensing length. The normalized capacitance variation per unit sensing length is defined as

$$S_{C,L} = \frac{C_{max} - C_{min}}{L}, \tag{13}$$

where C_{max} and C_{min} are the maximum and minimum capacitances over the investigated water-cut range, respectively, and L is the effective sensing length. $S_{C,L}$ represents the capacitance variation per unit effective sensing length over the full water-cut range, with units of pF/mm. This metric is used as a geometry-normalized indicator for comparing the capacitance response magnitudes of the three sensor configurations.

In summary, a comprehensive comparison of these metrics quantitatively evaluates different structural-parameter combinations regarding response capability and spatial uniformity, supporting structural-parameter optimization and selection.

Accordingly, S_{avg} is maximized and an appropriate capacitance ΔC is selected, whereas S_{dev} and S_{vp} are minimized during structural optimization. These four metrics were subsequently used to compare the orthogonal parameter combinations and determine the final structural configuration.

3.2 Orthogonal parameter simulation results and optimal structure determination

Simulation results were extracted using COMSOL Multiphysics. A comparative analysis of sensitivity metrics was conducted for nine orthogonal parameter combinations, with the results being summarized in Table 4. Overall, most combinations exhibited stable sensor output responses to variations in medium parameters. However, anomalous results occurred in certain parameter combinations.

Specifically, for Groups 4 and 7, when both the proportional coefficient p_1 and the helix radius r_1 were set to large values, the relative distance between the helix reservoir cross section and the electrodes significantly increased, leading to a marked attenuation of electric field strength within the detection region. Simulation results indicate that under these conditions, local potential distribution becomes highly distorted, resulting in negative calculated sensitivity values. Therefore, in subsequent parameter effect analysis and structural optimization, Groups 4 and 7 are excluded as non-physically valid operating conditions.

After excluding anomalous combinations, a comprehensive comparison of multi-indicators was conducted on the remaining parameter groups. As shown in Fig. 3, Groups 3, 5, 6, 8, and 9 showed no significant difference in average sensitivity, but exhibited distinct variations in

Table 4
Simulation verification results for nine orthogonal parameter combinations.

Test no.	Factor			S_{avg} (%)	S_{dvp} (%)	S_{vp} (%)	ΔC (pF)
	p_1	r_1 (mm)	N				
1	1.5	40	3	200.41	96.74	48	19.9
2	1.5	25	6	40.80	39.02	96	537.3
3	1.5	10	8	54.05	34.07	63	1783.8
4	3	40	6	−111.14	134.98	−121	21.7
5	3	25	8	52.27	34.64	66	649.6
6	3	10	3	56.48	33.28	59	422.3
7	5	40	8	−234.04	221.00	−94	10.7
8	5	25	3	50.37	35.29	70	134.6
9	5	10	6	56.06	33.43	60	494.5

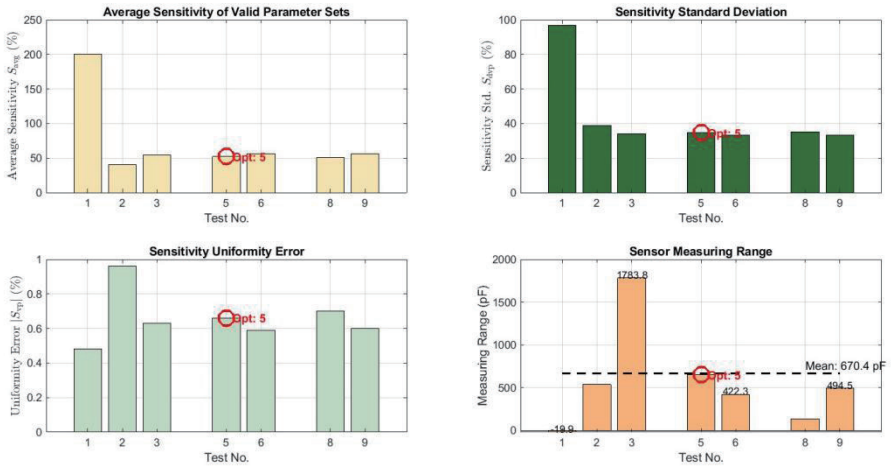


Fig. 3. (Color online) Analysis results of key metrics across different orthogonal experiments.

sensitivity standard deviation, uniformity error, and ΔC. Among these, Group 5 maintained a high average sensitivity while demonstrating a significantly superior measurement range compared with Group 6. Its sensitivity fluctuation level was comparable to those of Groups 3 and 9, indicating superior overall performance.

Considering key metrics such as average sensitivity, response stability, and measurement range, Group 5 was ultimately selected as the optimal parameter scheme for the HUS.

3.3 Simulation performance comparison of different sensor structures

To validate the performance advantages of the proposed helical uniform sensing structure, two optimized structures—an 8-electrode array and a counter-wall spiral electrode—were selected for comparison. Both were modeled using their optimized parameters to ensure fair and accurate comparison. The control variable method was employed in the simulation, where potential distribution and sensitivity response were analyzed by scanning oil–water volume ratios (water cut)[18–20] with the results indicated below.

The raw simulated capacitances of the three sensing structures under different water cuts are listed in Table 5. Variations in the volume fractions of oil and water phases directly alter the equivalent relative permittivity of the oil–water mixture, and this physical property parameter serves as the key factor governing the capacitance output response of the sensor.

To account for the effect of sensor dimensions on the capacitance response, the capacitances of the three sensing structures were normalized with respect to their effective sensing lengths. The 8-electrode structure and the opposite-wall helical structure have an effective sensing length of 180 mm, whereas the proposed HUS has an effective sensing length of 624 mm. On the basis of the normalized capacitance responses, the average sensitivity (S_{avg}), sensitivity standard deviation (S_{DVP}), sensitivity uniformity error (S_{VP}),and linearity coefficient (R^2) were used to compare the three structures. The results are summarized in Table 6.

Table 5
Simulated capacitance responses of three sensing structures at different water cuts.

water cut	8-electrode structure, C (pF)	Opposite-wall helical structure, *C* (pF)	HUS, *C* (pF)
0.0	24.5	47.3	1396.5
0.1	46.4	46.2	1447.7
0.2	68.4	46.1	1520.1
0.3	90.3	46.5	1599.7
0.4	112.2	47.1	1678.7
0.5	134.1	47.9	1753.8
0.6	156.0	48.7	1823.4
0.7	178.0	49.4	1887.2
0.8	199.9	50.1	1945.3
0.9	221.9	50.7	1998.2
1.0	243.8	51.3	2046.1

Table 6
Simulated performance metrics of three sensing structures.

Performance metric	8-electrode	Opposite-wall helical	HUS
S_{avg} (%)	50.00	25.50	52.27
S_{dev} (%)	33.17	46.32	34.64
S_{vp} (%)	66.34	181.64	66.27
Linearity (R^2)	1.0000	0.8726	0.9952
$S_{C,L}$ (pF/mm)	1.2181	0.0223	1.0410
ΔC (pF)	219.3	4.0	649.6

As shown in Table 6, the three structures exhibit distinctly different sensing characteristics. The 8-electrode structure provides a relatively large normalized capacitance variation of 1.2181 pF/mm and excellent linearity (R^2 = 1.0000). However, its average sensitivity is slightly lower than that of the proposed HUS. The opposite-wall helical structure exhibits a much smaller capacitance variation per unit length (0.02232 pF/mm), together with a lower average sensitivity of 25.50% and a significantly larger sensitivity uniformity error of 181.64%. These results indicate that its capacitance response to water-cut variation is relatively weak and spatially non-uniform.

In comparison, the proposed HUS achieves the highest average sensitivity of 52.27% while maintaining a sensitivity uniformity error of 66.27%, which is essentially comparable to that of the 8-electrode structure (66.34%). Moreover, the proposed HUS exhibits a high linearity coefficient of R^2 = 0.9952, indicating that its capacitance response remains highly correlated with water-cut variation. Although the normalized capacitance variation of the proposed HUS is slightly smaller than that of the 8-electrode structure, its average sensitivity is slightly higher while its sensitivity variation coefficient remains comparable.

Therefore, the proposed HUS was selected for subsequent investigation on the basis of its overall performance rather than a single optimization index. Its main advantage lies in the more uniform three-dimensional distribution of the sensing electrodes, which enables a larger portion of the sensing region to participate in the electric field interaction. This configuration provides a favorable balance among sensitivity, spatial response uniformity, and linearity. In addition, the helical arrangement extends the effective sensing path within the measurement region, allowing the sensing structure to maintain a strong capacitance response while avoiding the highly localized electric field interaction associated with conventional electrode arrangements. Consequently, the proposed HUS was adopted as the basic sensing structure for the subsequent structural optimization and experimental verification.

4. Test System Setup and Performance Validation

4.1 Test system setup and testing method

To experimentally verify the optimized HUS obtained from the simulations in Sect. 3, comparative tests were carried out using static oil-water mixtures.The static oil-water two-phase test system is shown in Fig. 4.

The HUS with optimized geometric parameters was fabricated and experimentally compared with a coaxial cylindrical sensor. Soybean oil and tap water were adopted as the oil and water phases, respectively. A graduated cylinder was used to measure corresponding volumes for preparing oil–water mixtures with water cut ranging from 0 to 1. Since this is a static experiment, no continuous flow velocity was applied. All tests were performed with the sensing region fully filled by the medium.

The experimental setup consists of the sensor, an FDC2214-based capacitance-to-digital converter measurement board, and a computer for data acquisition and storage. The support frame of the HUS sensor was manufactured by 3D printing, and aluminum foil was attached to the outer surfaces of the inner and outer spiral tubes to form the sensing electrodes. Heat-shrink tubing was sleeved on the outer side of the inner electrode for electrical insulation. The capacitance of the sensor was connected to the internal LC resonant circuit of the FDC2214. The measurement board was equipped with an inductor and a fixed capacitor. Changes in sensor capacitance alter the LC resonance characteristics, which are converted into digital measurement signals by the FDC2214 and transmitted to the computer via the serial port. A Python-based program was utilized for data acquisition and storage.

For each water-cut condition, the mixture was injected into the sensing region until it was completely filled, followed by a 5 min standing period to achieve system stability. Capacitance data were sampled approximately every 2 s, corresponding to a sampling rate of about 0.5 Hz. The final capacitance under each condition was obtained by averaging 50 consecutive measured readings. The measured capacitance responses were compared with simulation results to evaluate the response characteristics and linearity of the proposed HUS under static oil-water conditions.

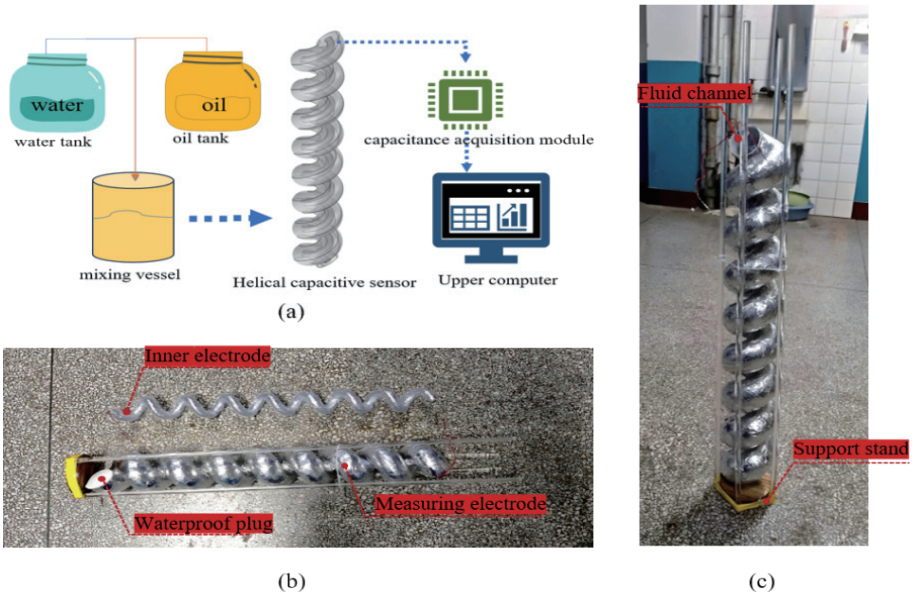


Fig. 4. (Color online) Oil-water two-phase test system and helical capacitive sensor prototypes. (a) Schematic of oil-water blending and testing platform. (b) Electrodes of the helical capacitive sensor. (c) Fully assembled sensing unit.

4.2 Analysis of test results and simulation consistency

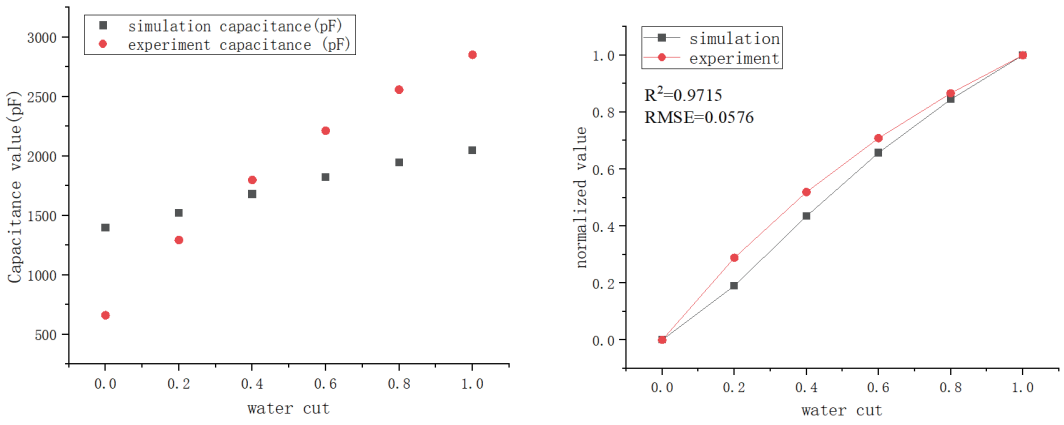
4.2.1 Comparison between simulation and experimental results

To experimentally evaluate the validity of the numerical model, the capacitance responses of the proposed HUS obtained from simulation and static oil–water experiments were compared at water cuts of 0, 0.2, 0.4, 0.6, 0.8, and 1.0. Figure 5(a) presents the corresponding absolute capacitances. Both the simulated and experimental capacitances increase monotonically with water cut, indicating that the numerical model correctly reproduces the overall response trend of the sensor. However, a notable difference exists between the absolute capacitances and response slopes. The simulated capacitance increases from 1396.5 to 2046.1 pF, whereas the experimental capacitance increases from 662.0 to 2850.9 pF.

To eliminate the effect of differences in absolute capacitance level and response amplitude, the simulation and experimental results were independently normalized according to

$$C_N = \frac{C - C_{min}}{C_{max} - C_{min}}, \tag{14}$$

where C_N is the normalized capacitance and C_{max} and C_{min} respectively denote the minimum and maximum capacitances within the corresponding dataset. The normalized results are shown in



(a) (b)

Fig. 5. (Color online) Comparison of simulated and experimental capacitance responses of the proposed HUS: (a) absolute and (b) normalized capacitance responses.

Fig. 5(b). The two curves exhibit similar overall variation characteristics over the investigated water-cut range. Quantitatively, the coefficient of determination between the normalized simulation and experimental results is R^2 = 0.9715, with an *RMSE* of 0.0576. These results indicate a high degree of agreement in the water-cut-dependent response characteristics predicted by the numerical model and observed experimentally.

The discrepancy in absolute capacitance can be attributed to several differences between the idealized numerical model and the practical measurement system, including fabrication tolerances, the actual dielectric properties and distribution of the oil–water mixture, parasitic capacitance, and the electrical characteristics of the measurement circuit. In particular, the simulation assumes an idealized electrode geometry and homogeneous material properties, whereas the experimental sensor and measurement circuit inevitably introduce additional parasitic effects. Therefore, the simulation is not expected to reproduce the absolute capacitances exactly. Nevertheless, the consistent monotonic response and high agreement of the normalized capacitance curves demonstrate that the developed numerical model can effectively predict the water-cut-dependent response of the proposed HUS.

4.2.2 Experimental comparison of the two sensing structures

Under the aforementioned experimental conditions, comparative testing was conducted on the output responses of HUS and the coaxial cylindrical structure at different water cuts. The results are shown in Table 7.

As shown in Fig. 6, both structures exhibit a monotonic increase in capacitance with water cut. The HUS provides a substantially larger absolute capacitance response than the coaxial cylindrical structure. Its capacitance increases from 662.0 to 2850.9 pF, corresponding to a capacitance variation of 2188.9 pF, whereas the coaxial cylindrical structure exhibits a variation of 66.6 pF. However, the absolute capacitance is inherently affected by sensor geometry, particularly the effective sensing length. Therefore, a direct comparison of the capacitances alone cannot fully characterize the structural advantage of the proposed sensor.

Table 7
Experimental capacitance responses of two sensing structures at different water cuts.

Water cut	Coaxial cylindrical structure measured effective average (pF)	HUS measured effective average (pF)
0.0	23.7	662.0
0.2	44.6	1293.2
0.4	60.3	1798.6
0.6	72.5	2212.8
0.8	82.3	2558.3
1.0	90.3	2850.9

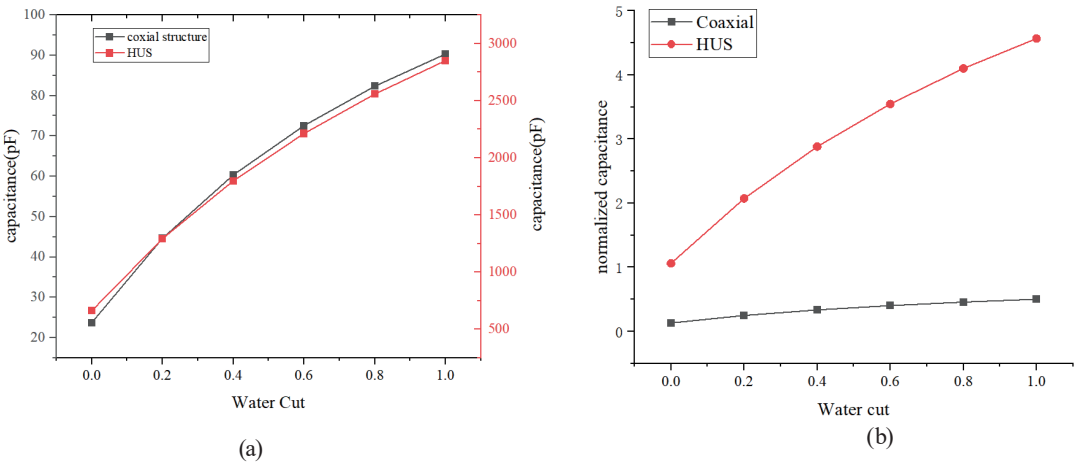


Fig. 6. (Color online) Experimental capacitance response vs water cut. (a) Absolute capacitance and (b) length-normalized capacitance responses.

After length normalization, the HUS still exhibits a substantially higher capacitance response per unit sensing length than the coaxial cylindrical structure. Over the full water-cut range, the normalized capacitance variation of the HUS is 3.5079 pF/mm, compared with 0.3702 pF/mm for the coaxial cylindrical structure.

To further evaluate the structural performance independently of the absolute capacitance, the average sensitivity, sensitivity variation, capacitance range, and linearity were calculated using the same definitions for both structures, as shown in Table 8.

The quantitative comparison results of the two sensing structures are summarized in Table 8. After normalization by the effective sensing length, the HUS exhibits a capacitance variation of 3.5079 pF/mm, which is approximately 9.5 times that of the coaxial cylindrical structure (0.3702 pF/mm). This result indicates that the stronger capacitance response of the HUS cannot be attributed solely to its larger sensing length.

In terms of sensitivity, the average sensitivity of the HUS is 56.38%, which is comparable to that of the coaxial structure (57.95%). The sensitivity standard deviations are also nearly identical at 37.38 and 37.36%, respectively, indicating comparable sensitivity consistency over the investigated water-cut range. Although the sensitivity variation coefficient of the HUS is slightly

Table 8
Experimental performance metrics of two sensing structures.

Indicator	Coaxial cylindrical structure	Helical uniformly distributed structure
$S_{C,L}$ (pF/mm)	0.3702	3.5079
S_{avg}	57.95%	56.38%
S_{dvp}	37.36%	37.38%
S_{VP}	64.47%	66.30%
R^2	0.9693	0.9803

higher (66.30% versus 64.47%), the difference is relatively small. Moreover, the HUS achieves a higher linearity, with an of $R^2 = 0.9803$, compared with 0.9693 for the coaxial structure.

Overall, the HUS provides a substantially larger capacitance variation per unit sensing length while maintaining sensitivity and sensitivity consistency comparable to those of the coaxial cylindrical structure. Its slightly higher linearity further indicates a favorable response to water-cut variation. These results demonstrate that the three-dimensional helical uniformly distributed electrode configuration improves the effective capacitance response of the sensor without significantly deteriorating the other key sensing characteristics.

4.3 Summary

Experimental tests were conducted to verify the numerical results and evaluate the sensing performance of the proposed HUS. The experimental results showed that the capacitance of the HUS increased monotonically with water cut, consistent with the trend predicted by the numerical model. After the independent normalization of the simulated and experimental capacitance responses, a high degree of agreement was obtained, demonstrating that the numerical model can effectively reproduce the water-cut-dependent response characteristics of the proposed structure.

Further comparison with the conventional coaxial cylindrical structure showed that the HUS provided a substantially larger capacitance variation after normalization by effective sensing length, reaching 3.5079 pF/mm compared with 0.3702 pF/mm for the coaxial structure. Moreover, the HUS maintained comparable average sensitivity and sensitivity consistency while achieving a slightly higher linearity ($R^2 = 0.9803$) than the coaxial structure ($R^2 = 0.9693$). These results indicate that the proposed three-dimensional helical uniformly distributed sensing configuration can provide a stronger capacitance response to watercut variation without the significant degradation of the overall sensing characteristics, demonstrating its potential for oil–water water-cut measurement.

5. Conclusions

A three-dimensional HUS was designed and optimized for capacitance-based oil–water water-cut measurement. The effects of the key geometrical parameters, including helical pitch, radial position, and the number of turns, were systematically investigated by COMSOL simulations and orthogonal parameter analysis. The optimized configuration was obtained with $r_1 = 25$ mm, $p_1 = 3$, and $N = 8$.

Comparative simulations with an 8-electrode structure and an opposite-wall helical structure demonstrated that the proposed HUS provides a favorable overall balance among sensitivity, sensitivity uniformity, capacitance response, and linearity. In particular, the uniformly distributed three-dimensional electrode configuration enhances the effective electrical interaction with the sensing region and provides a strong capacitance response to water-cut variation.

Experimental tests were subsequently conducted using static oil–water mixtures to verify the numerical model and evaluate the proposed sensor. The measured capacitance increased monotonically with water cut, consistent with the trend predicted by the simulations. After the independent normalization of the simulated and experimental responses, a high degree of agreement was obtained, confirming that the numerical model can effectively reproduce the water-cut-dependent response characteristics of the HUS.

Further experimental comparison with the conventional coaxial cylindrical structure showed that the HUS maintained a substantially larger capacitance variation after normalization by effective sensing length, with 3.5079 pF/mm compared with 0.3702 pF/mm for the coaxial structure. Moreover, the HUS exhibited comparable average sensitivity and sensitivity consistency, together with a slightly higher linearity R^2 = 0.9803 versus 0.9693. These results demonstrate that the proposed three-dimensional HUS can provide a stronger and more effective capacitance response to water-cut variation while maintaining favorable overall sensing characteristics, providing an experimental basis for its application in oil–water water-cut measurement.

Funding

This study received no funding.

Data availability statement

All the associated data are including within the manuscript.

Conflict of interest

There are no conflicts of interest.

References

1 C. Tan and F. Dong: Acta Automat. Sin. **39** (2013) 1923. https://doi.org/10.3724/SP.J.1004.2013.01923
2 H. Hu, K. Tang, C. Tang, and X. Wang: J. Northwest Univ. (Nat. Sci. Ed.) **49** (2019) 681. https://doi.org/10.16152/j.cnki.xdxbzr.2019-05-002
3 F. Hou: North China Electric Power University (Beijing) (2022). https://doi.org/10.27140/d.cnki.ghbbu.2022.001001
4 X. Wang, H. Hu, K. Tang, Y. Chen, and J. Pu: J. Northwest Univ. (Nat. Sci. Ed.) **49** (2019) 691. https://doi.org/10.16152/j.cnki.xdxbzr.2019-05-003
5 X. Wang, B. Wang, Y. Chen, and H. Hu: Acta Metrol. Sin. **41** (2020) 942.
6 X. X. Wang, H. L. Hu, X. Liu, and Y. Y. Zhang: Instrum. Sci. Technol. **43** (2015) 89. https://doi.org/10.1080/10739149.2014.963866

7 M. Zhang and M. Soleimani: Meas. Sci. Technol. **27** (2016) 025405. https://doi.org/10.1088/0957-0233/27/2/025405
8 H. Nugraha, D. Haryono, S. Harjanto, M. A. Huda, and W. P. Taruno: Phys. Scr. **98** (2023) 115033. https://doi.org/10.1088/1402-4896/ad008a
9 Y. Fan, H. Hu, F. Yang, and X. Yang: J. Xi'an Jiaotong Univ. **49** (2015) 110.
10 D. Liu: North China Electric Power University (Beijing) (2023). https://doi.org/10.27140/d.cnki.ghbbu.2023.000743
11 Q. Zeng, G. Li, Q. Liu, H. Jiang, and Z. Wang: Microw. Opt. Technol. Lett. **65** (2023) 47. https://doi.org/10.1002/mop.33451
12 B. A. Oommen and J. Philip: Int. J. Environ. Sci. Technol. **21** (2024) 3735. https://doi.org/10.1007/s13762-023-05218-8
13 J. Liu and M. Ai: Ind. Control Comput. **38** (2025) 30.
14 S. Liu: North China Electric Power University (Beijing) (2021). https://doi.org/10.27140/d.cnki.ghbbu.2021.000452
15 Z. Chen: Contemp. Chem. Ind. **51** (2022) 887. https://doi.org/10.13840/j.cnki.cn21-1457/tq.2022.04.018
16 X. Wang, J. Yan, H. Hu, X. Gao, and X. Zhang: J. Xi'an Jiaotong Univ. **47** (2013) 81.
17 H. Ji, K. Li, D. Song, W. Wang, B. Li, and W. Feng: Agric. Mech. Res. **47** (2025) 80. https://doi.org/10.13427/j.issn.1003-188X.2025.07.011
18 T. Wang, W. Zhou, and L. Wang: Int. J. Coal Prep. Util. **45** (2025) 1822. https://doi.org/10.1080/19392699.2024.2400618
19 L. G. Guo: Yangtze University (2023). https://doi.org/10.26981/d.cnki.gjhsc.2023.000426
20 K. Perera, W. A. S. Kumara, F. Hansen, S. Mylvaganam, and R. W. Time: Meas. Sci. Technol. **29** (2018) 065102. https://doi.org/10.1088/1361-6501/aab054

About the Authors



Haiming Xie is an associate professor at Xi'an Shiyou University's School of Electronic Engineering. He received his Ph.D. from Xidian University in 2018. His research focuses on downhole sensing and intelligent drilling technologies, including wireless data/power transmission, hydraulic system integration, and high-precision multiparameter measurement. He has also received several technology awards from CNOOC. (haimingxie@xsyu.edu.cn)



Rui Wang (Master's student, Class of 2024) received her B.Eng. degree from the School of Electronic Engineering, Xi'an Shiyou University, Xi'an, China, in 2024. She is currently pursuing an M.S. degree in instrument science and technology at the same university. Her research since 2024 has focused on capacitive sensors for oil–water two-phase flow. (2302763744@qq.com)



Jianqiang Huang (Master's student, Class of 2024) received his BEng degree from the School of Communication and Information Engineering, Chongqing College of Mobile Communication in 2023. Currently, he is a postgraduate student majoring in next-generation electronic information technology at Xi'an Shiyou University, researching high-temperature power supplies for downhole oil wells. (2785076506@qq.com)